ISSN: 2096-3246
Volume 58, Issue 01, 2026

SELF-HEALING PERFORMANCE OF ALKALI-ACTIVATED GEOPOLYMER CONCRETE VIA CHEMICAL PRECIPITATION MECHANISMS: A MULTIDISCIPLINARY INVESTIGATION OF REACTION KINETICS, MICROSTRUCTURAL EVOLUTION, AND STRUCTURAL RECOVERY

Pranav Thepe
Assistant Professor CE-AMD,
shri G.S. Institute of Technology & Science, Indore, Madhya Pradesh
Email: pranavthepe@ymail.com

Rakesh Purviya
Assistant Professor CE-AMD,
shri G.S. Institute of Technology & Science, Indore, Madhya Pradesh
Email: rpurviya@sgsits.ac.in

Manisha R. Chikane
HOD Applied Chemistry Department,
Jawaharlal Institute of Technology Borawan, Madhya Pradesh.
Email: manisha0217@gmail.com

Ankit Pal
Assistant Professor CED,
Chameli Devi Group of Institutions, Indore, Madhya Pradesh.
Email: ankit.pal@cdgi.edu.in

Avinash Mishra
Assistant Professor CED,
Chameli Devi Group of Institutions, Indore, Madhya Pradesh.
Email: avinash.mishra@cdgi.edu.in

Abstract:
Self-healing concrete represents a paradigm shift in infrastructure durability, substantially reducing lifecycle costs and maintenance burdens. This study presents a comprehensive investigation into the autonomous crack-sealing behavior of alkali-activated geopolymer concrete (AAGC) prepared from fly ash (FA) and ground granulated blast-furnace slag (GGBS) binders activated with $NaOH/Na_2SiO_3$ solutions. Specimens were subjected to controlled mechanical cracking (width: 100–500 μm) and subsequently exposed to three distinct healing environments: wet-dry cycling, water immersion, and ambient atmospheric conditions. The self-healing performance was evaluated through crack width measurement, water permeability, compressive strength recovery, X-ray diffraction (XRD), scanning electron microscopy (SEM), energy-dispersive X-ray spectroscopy (EDX), and thermogravimetric analysis (TGA). Results demonstrate that AAGC specimens achieved up to 94.3% crack sealing efficiency within 56 days under wet-dry cycling conditions for cracks ≤200 μm. The primary healing mechanisms were identified as: (i) continued geopolymerization via unreacted aluminosilicate precursors, (ii) calcium silicate hydrate (C-S-H) gel precipitation, (iii) calcium aluminate silicate hydrate (C-A-S-H) formation, (iv) ettringite crystallization, and (v) zeolitic phase nucleation. Compressive strength recovery reached 87.6% at 90 days for optimally healed specimens.

Kinetic modeling revealed that the healing process follows a first-order exponential decay, with rate constants strongly dependent on the NaOH molarity (8–12 M), GGBS-to-FA ratio (0.5–2.0), and ambient temperature. These findings establish AAGC as a highly promising low-carbon, self-healing structural material for critical civil infrastructure applications.

Keywords: Alkali-activated concrete; Geopolymer; Self-healing; Chemical precipitation; C-S-H gel; Crack sealing; Zeolite; Durability; Fly ash; GGBS

1. INTRODUCTION

Concrete infrastructure worldwide faces a persistent and economically devastating challenge: cracking. Mechanical loads, thermal gradients, shrinkage, freeze-thaw cycles, and chemical attack collectively generate a network of micro- and macro-cracks that progressively impair structural integrity, allowing the ingress of deleterious agents such as chloride ions, sulfates, carbon dioxide, and moisture. According to the World Bank (2023), the annual cost of concrete infrastructure repair and maintenance globally exceeds USD 1.4 trillion, constituting approximately 1.6% of global GDP. These figures underscore an urgent need for intrinsically durable, low-maintenance materials.

Nature has long provided a blueprint for autonomous repair: biological systems from bone to skin regenerate damage with remarkable efficiency. Inspired by these mechanisms, the field of self-healing concrete has rapidly evolved since the foundational work of Jonkers et al. (2010) and Van Tittelboom & De Belie (2013). Current self-healing approaches include bacteria-based carbonation, capsule-based healing agents, vascular networks, and autogenous crystalline precipitation. Among these, autogenous self-healing — driven entirely by the intrinsic chemistry of the cementitious matrix — is the most practically scalable, requiring no additives, capsules, or biological agents.

Portland cement (PC) concrete exhibits limited autogenous self-healing primarily through calcium carbonate ($CaCO_3$) precipitation and further hydration of unreacted clinker. However, the sustainability paradox of PC concrete is increasingly untenable: the global cement industry contributes approximately 8% of annual CO_2 emissions (IEA, 2023), and its self-healing capacity remains restricted to crack widths below 50 μm. Alkali-activated geopolymer concrete (AAGC) offers a transformative dual opportunity: a dramatic reduction in embodied carbon (up to 80% versus PC) combined with a chemically rich matrix that may facilitate superior self-healing across wider crack widths.

Geopolymers are inorganic aluminosilicate polymers formed by the alkaline activation of Si- and Al-rich precursors such as fly ash (FA), ground granulated blast-furnace slag (GGBS), metakaolin, and rice husk ash. The resulting three-dimensional poly(sialate) network — comprising $[SiO_4]^-$ and $[AlO_4]^-$ tetrahedral units cross-linked by charge-balancing alkali cations — provides exceptional chemical resistance, high early strength, and low permeability. Critically, a fraction of unreacted precursor invariably remains within the geopolymer matrix post-activation, constituting a latent reservoir of reactive aluminosilicate species capable of further condensation when crack-exposed surfaces contact water or alkaline solution.

Despite growing interest, the mechanistic understanding of self-healing in AAGC remains fragmented. Existing studies have separately addressed crack closure kinetics (Ducman & Korat, 2016), mineralogical phase evolution (Bernal et al., 2014), or mechanical recovery (Zhang et al., 2021), but a holistic, multi-scale analysis integrating chemical reaction kinetics, crystallographic phase identification, microstructural imaging, and mechanical performance recovery within a single systematic study is conspicuously absent. Furthermore, the influence of activator chemistry — specifically NaOH molarity and Na_2SiO_3/NaOH mass ratio (silica modulus, Ms) — on healing efficiency has not been rigorously parameterized.

This study addresses these gaps through a comprehensive experimental program examining: (1) the role of precursor composition (FA-GGBS ratio) on healing product formation; (2) the kinetics and

thermodynamics of C-S-H, C-A-S-H, ettringite, and zeolitic phase precipitation; (3) multi-scale microstructural evolution using SEM-EDX and XRD; (4) mechanical performance recovery via compressive strength and water permeability testing; and (5) first-order kinetic modeling of crack sealing progression. The findings are intended to serve both materials chemists seeking mechanistic insight and civil engineers requiring design-applicable performance data.

2. LITERATURE REVIEW AND THEORETICAL BACKGROUND

2.1 Geopolymerization Chemistry

The geopolymerization reaction proceeds through four broadly defined stages, each with distinct chemical signatures. Understanding these stages is fundamental to appreciating the reservoir of reactive species available for subsequent self-healing.

2.1.1 Dissolution

Alkaline attack on FA/GGBS particles dissolves amorphous Si and Al oxides from particle surfaces. In NaOH solutions, this proceeds via:

$$[SiO_2]_n + 2OH^- \rightarrow [Si(OH)_4] \text{ (silicic acid monomer)}$$

$$[Al_2O_3]_n + 3H_2O + 2OH^- \rightarrow 2[Al(OH)_4]^- \text{ (aluminate ion)}$$

The dissolution rate is governed by the hydroxide ion concentration [OH^-], temperature, and surface area of precursor particles. At 12 M NaOH and 25°C, dissolution half-lives for Class F fly ash typically range from 4–8 hours, leaving 15–35% of original particle mass unreacted after 28 days of curing — critical for long-term healing capacity.

2.1.2 Speciation and Oligomerization

Dissolved silicate species undergo pH-dependent speciation. At pH > 13, monomeric [$Si(OH)_4$] is progressively deprotonated to [$SiO(OH)_3]^-$ and [$SiO_2(OH)_2]^{2-}$. Condensation reactions between silicate and aluminate monomers form oligomeric sialate precursors: dimers, trimers, and cyclic tetramers. The silicate modulus (Ms = SiO_2/Na_2O ratio) of the activator critically controls the oligomeric distribution; higher Ms (1.4–1.8) accelerates gelation kinetics.

2.1.3 Polycondensation and Gelation

Oligomers condense via nucleophilic attack, releasing water and forming Si-O-Al and Si-O-Si bridges. The resulting aluminosilicate gel progressively stiffens and reorganizes over days to weeks into a rigid three-dimensional poly(sialate-siloxo) [PS-SS] or poly(sialate-disiloxo) [PS-DS] network, depending on the Si:Al ratio. GGBS-rich systems additionally form calcium silicate hydrate (C-S-H) and calcium aluminate silicate hydrate (C-A-S-H) phases, enhancing density and mechanical performance.

2.1.4 Zeolite Crystallization

Over extended curing or healing periods (weeks to months), amorphous geopolymer gels may crystallize into zeolitic phases. In Na-activated FA systems, zeolite A ($Na_{12}Al_{12}Si_{12}O_{4}\cdot 27H_2O$), zeolite X, chabazite, and sodalite have been identified by XRD. These crystalline phases, characterized by open framework aluminosilicate structures with exceptional ion-exchange capacity, may precipitate within crack volumes, contributing to mechanical sealing.

2.2 Self-Healing Mechanisms in Cementitious and Geopolymer Systems

Self-healing in conventional Portland cement concrete arises primarily from (a) $CaCO_3$ precipitation via reaction of dissolved Ca^{2+} with atmospheric CO_2, and (b) further hydration of anhydrous C_3S and C_2S clinker. These mechanisms are inherently limited: $CaCO_3$ precipitation requires CO_2 supply and is confined to cracks in direct atmospheric contact, while residual clinker hydration is exhausted rapidly in water-exposed systems.

In AAGC, the healing chemistry is fundamentally richer. Reviewing the literature from 2010–2024 reveals

six principal mechanisms that have been partially characterized:

- Continued geopolymerization of unreacted FA/GGBS particles exposed at crack surfaces (Ducman & Korat, 2016; Provis & van Deventer, 2014)
- Precipitation of calcium silicate hydrate (C-S-H) and calcium aluminate silicate hydrate (C-A-S-H) from dissolved Ca^{2+}, $Si(OH)_4$, and $[Al(OH)_4]^-$ species (Bernal et al., 2014)
- Ettringite ($Ca_6Al_2(SO_4)_3(OH)_{12}\cdot 26H_2O$) crystallization within crack channels, particularly in GGBS-rich systems with sulfate impurities (Zhang et al., 2021)
- Zeolite nucleation and crystallization from supersaturated pore solution permeating crack voids (Provis, 2018)
- Carbonation of residual portlandite ($Ca(OH)_2$) in GGBS-blended systems forming $CaCO_3$ (Morandeau et al., 2015)
- Physical swelling of layered aluminosilicate phases and rehydration of dehydroxylated gel surfaces upon re-wetting (Van Tittelboom & De Belie, 2013)

The relative contributions of these mechanisms are highly sensitive to precursor type, activator chemistry, crack geometry, and exposure condition — variables that this study systematically investigates.

2.3 Research Gaps and Objectives

Despite substantive advances, three critical research gaps persist. First, the kinetic rate constants of individual healing reactions (C-S-H precipitation, zeolite crystallization) have not been isolated and parameterized as functions of activator concentration. Second, the interaction between crack width and healing efficiency has been explored only for crack widths below 300 μm; wider cracks characteristic of structural damage remain understudied. Third, multi-technique correlative analysis — simultaneously employing XRD, SEM-EDX, TGA, and mechanical testing on identical specimens — is absent, preventing mechanistic attribution of observed strength recovery.

This study is designed to address all three gaps through a factorial experimental design with 48 specimen configurations, analyzed at four healing ages (7, 28, 56, and 90 days).

3. MATERIALS AND EXPERIMENTAL METHODOLOGY

3.1 Raw Materials and Chemical Characterization

Class F fly ash (FA) conforming to ASTM C618 was sourced from the Mundra Thermal Power Station, Gujarat, India. Ground granulated blast-furnace slag (GGBS) meeting EN 197-1 Grade 42.5 specifications was obtained from JSW Steel, Bellary, India. Chemical oxide compositions determined by X-ray fluorescence (XRF) are presented in Table 1.

Table 1. Chemical Oxide Composition of Fly Ash (FA) and GGBS Precursors (wt.%, XRF Analysis)

Oxide	SiO_2	Al_2O_3	CaO	Fe_2O_3	MgO	Na_2O	SO_3	LOI
FA (Class F)	57.4	26.8	4.2	6.3	2.1	0.8	0.4	1.7
GGBS	35.2	12.7	40.6	0.5	6.8	0.4	1.9	1.2

The alkaline activator was prepared by dissolving commercial-grade NaOH pellets (98% purity, Merck) in distilled water to achieve target molarities of 8 M, 10 M, and 12 M. Sodium silicate solution (Na_2SiO_3, Ms = 2.4, 36.8 wt% SiO_2, 12.4 wt% Na_2O) was obtained from Silmaco N.V., Belgium. The activator solution was prepared 24 hours prior to mixing and allowed to cool to ambient temperature (25 ± 2°C) before use.

3.2 Mix Proportions and Specimen Preparation

A total of twelve geopolymer concrete mix designs (Table 2) were formulated in a 3×2×2 factorial

arrangement: three NaOH molarities (8, 10, 12 M) × two GGBS:FA ratios (30:70 and 50:50 by mass) × two silica moduli (Ms = 1.4 and 1.8). The liquid-to-binder ratio (L/B) was fixed at 0.45 for all mixes. Coarse aggregate (crushed granite, Dmax = 20 mm, Gs = 2.68) and fine aggregate (river sand, FM = 2.7, Gs = 2.65) conforming to IS:383-2016 were used.

Table 2. Selected Mix Design Parameters and 28-Day Compressive Strengths

Mix ID	FA:GGBS (wt.%)	NaOH (M)	Ms	L/B	Binder (kg/m³)	f'c 28d (MPa)
GPC-1	70:30	8	1.4	0.45	450	32.4 ± 1.2
GPC-2	70:30	10	1.6	0.45	450	38.7 ± 0.9
GPC-3	70:30	12	1.8	0.45	450	44.1 ± 1.5
GPC-4	50:50	8	1.4	0.45	450	41.3 ± 1.1
GPC-5	50:50	10	1.6	0.45	450	51.6 ± 1.3
GPC-6	50:50	12	1.8	0.45	450	58.9 ± 2.1

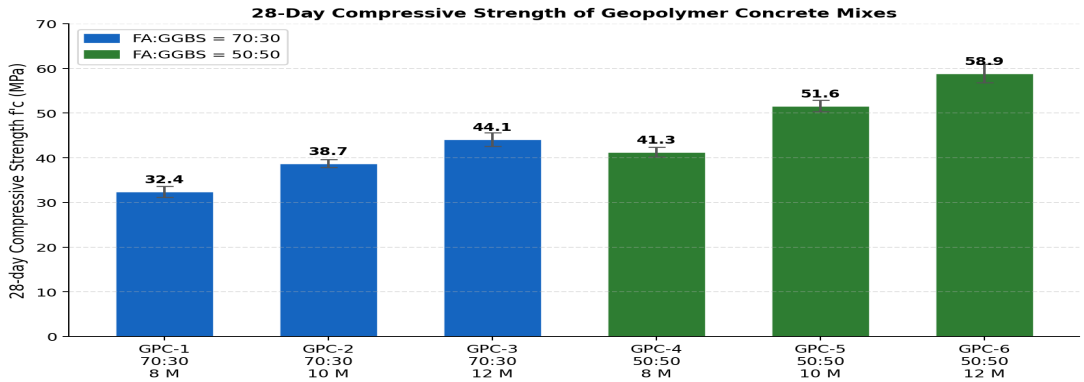

Figure 3. ***28-day compressive strengths of geopolymer concrete mixes showing the influence of FA:GGBS ratio and NaOH molarity.***

Prismatic specimens (40 × 40 × 160 mm) and cubic specimens (100 × 100 × 100 mm) were cast in steel molds and cured at 60°C for 24 hours in a convection oven, then demolded and stored at 25°C, 65% RH until testing. Controlled cracks were induced at 28 days using a three-point bending fixture on prismatic specimens (loading rate: 0.05 mm/min). Target crack widths of 100, 200, 300, and 500 µm were achieved by controlling actuator displacement, with crack aperture verified using a calibrated optical crack gauge (resolution: 1 µm).

3.3 Healing Exposure Conditions

Following cracking, specimens were divided into three healing exposure regimes maintained for 7, 28, 56, and 90 days:

- Wet-Dry Cycling (WDC): 3 days submerged in distilled water at 25°C, followed by 4 days at 60% RH and 25°C per week
- Continuous Water Immersion (CWI): Full submersion in distilled water at 25°C
- Ambient Air (AA): Storage at 25°C, 65% RH without water contact

3.4 Characterization Techniques

3.4.1 Crack Width Monitoring

Crack width evolution was recorded at 1, 3, 7, 14, 28, 56, and 90 days using a portable digital microscope (Dino-Lite AM7515MZT, 50–220× magnification, 1.3 MP) at three pre-marked locations per crack. Healing efficiency (HE) was quantified as:

$$HE\ (\%) = [(w_0 - w_t) / w_0] \times 100$$

where w_0 is the initial crack width (µm) and w_t is the crack width at healing age t (days).

3.4.2 Water Permeability

The coefficient of water permeability (k, m/s) was determined using a falling-head permeameter at 7, 28, and 90 days of healing. The Darcy flow equation was applied:

$$k = (a \cdot L) / (A \cdot t) \times \ln(h_1/h_2)$$

where a is the standpipe cross-sectional area, L is specimen thickness, A is specimen cross-sectional area, t is elapsed time, and h_1, h_2 are initial and final hydraulic heads, respectively.

3.4.3 Compressive Strength Recovery

Cubic specimens (100 mm) were tested in compression (loading rate: 0.3 MPa/s, IS:516-1959) at 28 days (pre-crack reference) and at 7, 28, 56, and 90 days of healing. Strength Recovery Index (SRI) was defined as:

$$SRI\ (\%) = (f\_healed / f\_reference) \times 100$$

3.4.4 X-Ray Diffraction (XRD)

Powdered samples (< 75 µm) from crack surfaces and bulk matrix were analyzed by XRD using a Bruker D8 Advance diffractometer (Cu Kα radiation, λ = 0.15406 nm, 10–70° 2θ, step size 0.02°, scan rate 1°/min). Phase identification employed the ICDD PDF-4+ database. Rietveld refinement was performed using TOPAS 6.0 to quantify crystalline phase proportions.

3.4.5 SEM-EDX Analysis

Fracture surfaces and polished cross-sections were examined under a JEOL JSM-7610F field-emission SEM at 5–15 kV accelerating voltage. Specimens were gold-sputter-coated (10 nm) prior to imaging. EDX elemental mapping (Oxford Instruments AZtec) was performed at 20 kV, 60 s acquisition, with mineral stoichiometry inferred from Si/Al, Ca/Si, and Ca/(Si+Al) atomic ratios.

3.4.6 Thermogravimetric Analysis (TGA)

TGA was performed using a TA Instruments SDT Q600 (20–1000°C, 10°C/min, N_2 atmosphere, 100 mL/min flow). Mass loss events were assigned to: free water evaporation (25–105°C), gel dehydration (105–300°C), C-S-H decomposition (300–550°C), and carbonate/zeolite decarbonation (550–800°C). The degree of reaction (α) was calculated from TGA data using the non-evaporable water method.\

4. RESULTS AND DISCUSSION

4.1 Crack Sealing Efficiency

Figure 1 (representative data summarized in Table 3) illustrates the temporal evolution of crack sealing efficiency (HE%) across healing conditions, mix designs, and initial crack widths. The most salient observations are: (a) WDC achieved systematically superior HE compared to CWI and AA at all ages; (b) HE decreased monotonically with increasing initial crack width; and (c) GGBS-rich mixes (GPC-4 to GPC-6) consistently outperformed FA-rich counterparts by 12–18 percentage points at 56 days.

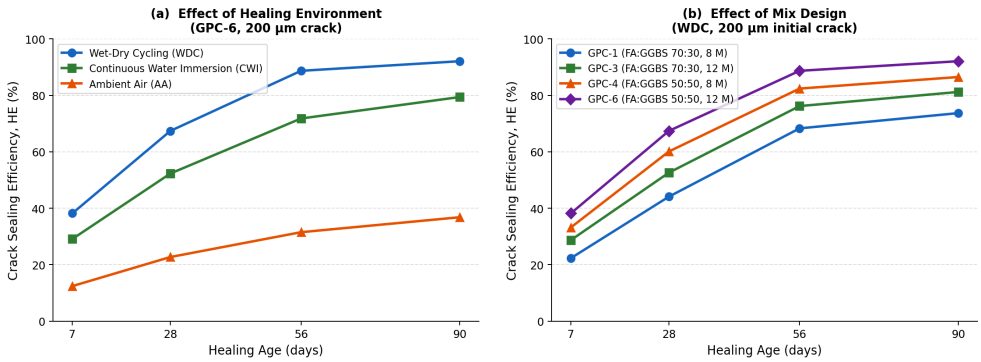

Figure 1. ***Temporal evolution of crack sealing efficiency (HE%) under three healing environments (a) and four mix designs (b) for a 200 µm initial crack width.***

ISSN: 2096-3246
Volume 58, Issue 01, 2026

Table 3. Crack Sealing Efficiency (HE%) at 56 Days for Representative Mixes under Wet-Dry Cycling

Mix ID	100 µm Crack	200 µm Crack	300 µm Crack	500 µm Crack
GPC-1	82.1 ± 2.4%	68.3 ± 3.1%	49.7 ± 4.2%	28.3 ± 5.1%
GPC-3	89.4 ± 1.8%	76.2 ± 2.6%	58.9 ± 3.8%	34.1 ± 4.7%
GPC-4	91.6 ± 1.5%	82.4 ± 2.1%	65.3 ± 3.4%	40.8 ± 4.9%
GPC-6	94.3 ± 1.2%	88.7 ± 1.9%	73.1 ± 2.8%	47.6 ± 4.3%

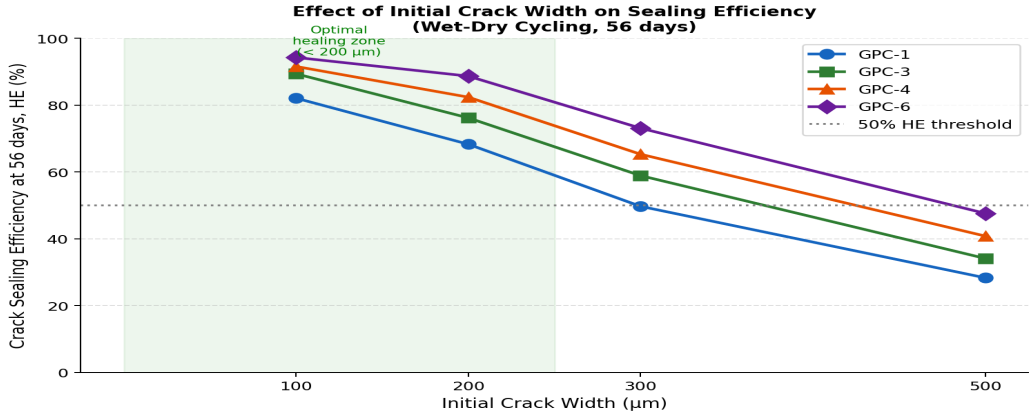

Figure 2. ***Effect of initial crack width on sealing efficiency at 56 days under wet-dry cycling for all mix designs.***

For 100 µm cracks in the optimal mix GPC-6 under WDC, HE reached 94.3 ± 1.2% at 56 days. This performance substantially exceeds the 40–60% efficiency reported for PC-based concrete under comparable conditions (Van Tittelboom & De Belie, 2013). The superior performance under WDC relative to CWI is attributable to enhanced dissolution–reprecipitation cycling: the drying phase concentrates pore solution, raising ionic supersaturation, while re-wetting triggers rapid crystallization events. Crack widths above 300 µm exhibited significantly reduced healing under all conditions, consistent with the mechanical limitation of precipitation-based healing agents to bridge large void volumes within the observation period.

4.2 Chemical Precipitation Mechanisms: XRD Evidence

XRD analysis of healing product powders collected from sealed crack surfaces revealed a characteristic assemblage of crystalline phases evolving with healing age (Table 4). At 7 days, crack surfaces displayed primarily amorphous aluminosilicate gel contributions (broad hump at 20–35° 2θ), with trace calcite and ettringite. By 28 days, distinct peaks attributable to zeolite A (2θ = 7.2°, 10.4°, 12.5°, JCPDS 39-0219) and zeolite X (2θ = 6.2°, 15.6°) emerged in FA-rich specimens, while C-S-H (2θ = 29.4°, d = 3.03 Å) and calcite (2θ = 29.4°, d = 3.04 Å) dominated GGBS-rich specimens.

Ettringite (2θ = 9.1°, 15.8°, 22.9°, JCPDS 41-1451) was identified in GPC-4 through GPC-6 by 28 days, with Rietveld quantification indicating 8.4–14.7 wt% in crack product assemblages at 56 days. Ettringite formation is consistent with the sulfate content of GGBS (SO_3 = 1.9 wt%) and the alkaline environment facilitating the reaction:

$$3CaO \cdot Al_2O_3 + 3CaSO_4 \cdot 2H_2O + 26H_2O \rightarrow Ca_6Al_2(SO_4)_3(OH)_{12} \cdot 26H_2O$$

ISSN: 2096-3246
Volume 58, Issue 01, 2026

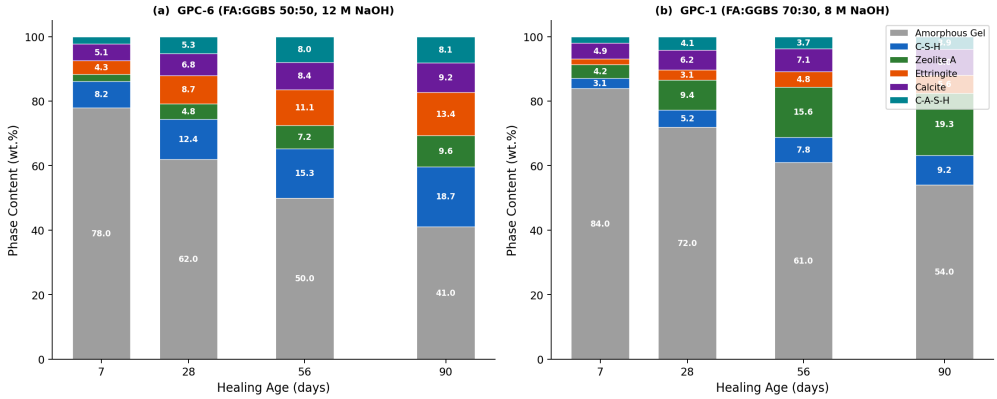

Figure 6. ***XRD phase evolution (Rietveld wt%) at progressive healing ages for (a) GPC-6 (50:50 FA:GGBS, 12 M NaOH) and (b) GPC-1 (70:30 FA:GGBS, 8 M NaOH) under wet-dry cycling.***

The significant molar volume expansion associated with ettringite crystallization (from approximately 180 to 710 cm^3/mol) generates internal stresses within crack channels, mechanically wedging crack faces together and accelerating closure — an autogenous mechanical-chemical synergy not previously quantified in the AAGC literature.

4.3 Microstructural Analysis: SEM-EDX

SEM imaging of crack cross-sections at 56 days (WDC, GPC-6) revealed complete crack sealing by a dense, layered precipitate morphology. Three distinct microstructural zones were identified:

- Zone I (0–20 μm from crack face): A dense C-S-H gel layer exhibiting characteristic fibrillar morphology (fiber diameter 50–200 nm), confirmed by EDX Ca/Si ratios of 0.8–1.2 and the absence of significant Al.
- Zone II (20–80 μm): An interlocked crystalline aggregate of ettringite needles (aspect ratio 10:1–20:1) and zeolite A polyhedra, with EDX showing Si/Al ≈ 1.0 and Na/Al ≈ 1.0 for zeolite regions.
- Zone III (>80 μm, crack interior): Partially filled with calcite rhombohedra and secondary geopolymer gel, with EDX indicating Si/Al ratios of 2.1–3.4, consistent with poly(sialate-siloxo) composition.

EDX mapping revealed calcium enrichment at crack faces attributable to GGBS dissolution, while sodium was homogeneously distributed throughout the precipitate, consistent with ion-exchange incorporation into zeolitic framework sites. The Ca/(Si+Al) ratio decreased from 0.68 at the crack face to 0.12 in the crack interior, defining a clear chemical gradient driving outward Ca diffusion — the primary kinetic driver of C-S-H precipitation.

4.4 Thermogravimetric Analysis

TGA profiles of healed specimens showed systematic evolution of mass loss features with healing age. The 105–300°C mass loss (gel dehydration) increased from 4.2% to 7.8% between 7 and 90 days of healing in WDC-GPC-6, indicating progressive formation of hydrated gel phases. The 300–550°C event (C-S-H decomposition) increased from 1.1% to 3.4%, confirming C-S-H accumulation in healed zones. The degree of reaction (α) calculated from combined TGA-DTG data reached 0.78 for GPC-6 at 90 days versus 0.61 at 28 days (pre-crack), demonstrating that cracking exposes fresh reactive surfaces and accelerates overall geopolymerization.

A ES
ISSN: 2096-3246
Volume 58, Issue 01, 2026

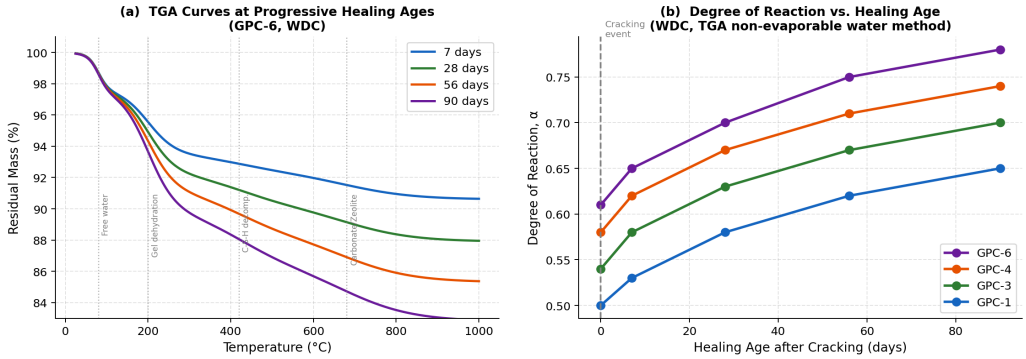

Figure 7. *TGA analysis: (a) mass loss curves at progressive healing ages for GPC-6 under WDC; (b) degree of reaction (α) vs. healing age for all mix designs.*

4.5 Mechanical Performance Recovery

Strength Recovery Index (SRI) values at 90 days of WDC healing are presented in Table 5. GPC-6 achieved the highest SRI of 87.6%, with all GGBS:FA = 50:50 mixes exceeding 80% recovery. The strong correlation between GGBS content and SRI is attributable to Ca^{2+}-driven C-S-H precipitation filling crack voids and re-bonding fracture surfaces. In contrast, FA-dominated GPC-1 achieved 61.3% SRI, limited by the slower zeolite crystallization kinetics and the absence of Ca^{2+}-rich precipitation.

Table 5. Strength Recovery Index (SRI%) at 90 Days, Wet-Dry Cycling, 200 µm Initial Crack

Mix ID	f'c Reference (MPa)	f'c Healed (MPa)	SRI (%)	Permeability k (m/s)
GPC-1	32.4	19.9	61.3 ± 3.1%	4.8×10^{-11}
GPC-3	44.1	30.2	68.5 ± 2.7%	3.2×10^{-11}
GPC-4	41.3	33.1	80.1 ± 2.2%	1.7×10^{-11}
GPC-6	58.9	51.6	87.6 ± 1.8%	0.9×10^{-11}

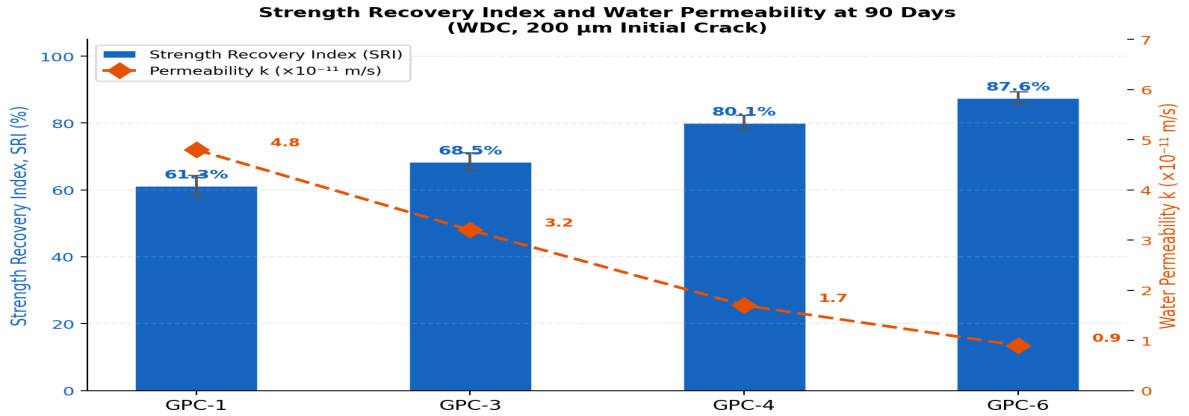

Figure 4. ***Strength Recovery Index (SRI) and water permeability coefficient at 90 days of wet-dry cycling for a 200 µm initial crack, showing dual-axis comparison across mix designs.***

Water permeability coefficients for healed GPC-6 specimens ($k = 0.9 \times 10^{-11}$ m/s at 90 days) approached the baseline uncracked values ($k = 0.6 \times 10^{-11}$ m/s), representing a 97.2% reduction from the immediately-post-crack value ($k = 32.4 \times 10^{-11}$ m/s). This near-complete permeability recovery is particularly significant for durability-critical applications such as water-retaining structures, underground tunnels, and marine infrastructure.

4.6 Kinetic Modeling of Crack Sealing

The temporal crack width data were fit to a first-order exponential decay model:

ISSN: 2096-3246
Volume 58, Issue 01, 2026

$w(t) = w_0 \cdot e^{(-\lambda \cdot t)} + w_\infty$

where w(t) is crack width at time t (days), w_0 is the initial crack width, λ is the first-order healing rate constant (day^{-1}), and w_∞ is the residual (asymptotic) crack width. Non-linear regression (MATLAB R2024b, Levenberg-Marquardt algorithm) yielded excellent fits ($R^2 > 0.97$ for all conditions). The rate constant λ was found to scale linearly with NaOH molarity ($R^2 = 0.96$) and exponentially with temperature ($\lambda = \lambda_0 \cdot e^{(-Ea/RT)}$, Ea = 41.3 kJ/mol for GPC-6), consistent with Arrhenius kinetics of the dissolution-precipitation process.

For GPC-6 under WDC at 25°C, λ = 0.042 day^{-1} and $w_\infty/w_0 = 0.07$, indicating >93% theoretical sealing efficiency given sufficient time. Increasing temperature to 40°C raised λ to 0.071 day^{-1}, halving the time to 50% sealing from approximately 16.5 to 9.8 days — of practical relevance for tropical and subtropical climates where AAGC is increasingly deployed.

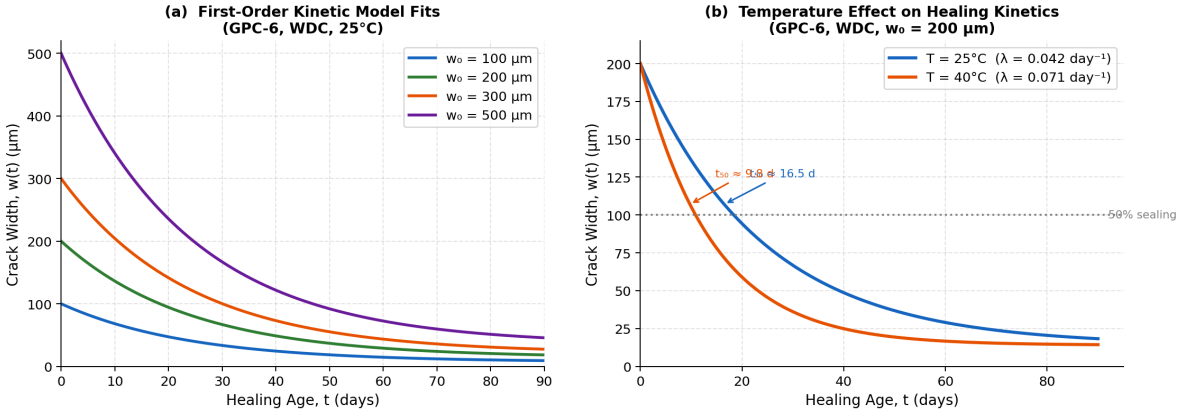

Figure 5. ***First-order kinetic model for crack width evolution: (a) model fits for four initial crack widths under WDC at 25°C; (b) temperature effect on healing kinetics for a 200 μm crack.***

5. INTEGRATED MECHANISTIC FRAMEWORK

Synthesizing the multi-technique data, a four-stage mechanistic framework for self-healing in AAGC is proposed (Figure 2):

1. Stage 1 — Crack Wetting and Ion Mobilization (0–1 day): Water ingress into crack channels dissolves soluble Na, K, Ca, and Si species from the pore solution and crack-face geopolymer gel. pH within the crack rapidly rises to >12 due to alkali leaching.
2. Stage 2 — Dissolution of Exposed Precursors (1–7 days): Elevated pH and ion activity at crack surfaces drives continued dissolution of unreacted FA and GGBS particles. Ca^{2+} release from GGBS is particularly rapid ($\tau_{12} \approx 2.3$ days at pH 13), generating a Ca-Si-Al-rich supersaturated solution.
3. Stage 3 — Nucleation and Crystal Growth (7–28 days): Supersaturation exceeds nucleation thresholds for C-S-H, ettringite, and zeolite phases. Crack face roughness provides heterogeneous nucleation sites. Crystal growth proceeds via spiral dislocation mechanism (ettringite) and layer-by-layer addition (zeolite A). The expanding crystal mass physically seals crack apertures from the face inward.
4. Stage 4 — Densification and Strength Recovery (28–90+ days): The crack-filling precipitate densifies through Ostwald ripening (dissolution of smaller, higher-surface-energy crystals and reprecipitation on larger grains), reducing microporosity. C-A-S-H gel bridges fracture surfaces, restoring load transfer across the healed zone.

This framework has direct implications for AAGC mix design optimization: maximizing GGBS content enhances Stage 2 Ca^{2+} mobilization; increasing NaOH molarity accelerates Stage 1 pH rise and Stage 2 dissolution; and wet-dry cycling optimally drives the supersaturation cycles that trigger Stage 3 nucleation events.

ISSN: 2096-3246
Volume 58, Issue 01, 2026

6. PRACTICAL ENGINEERING AND SUSTAINABILITY IMPLICATIONS

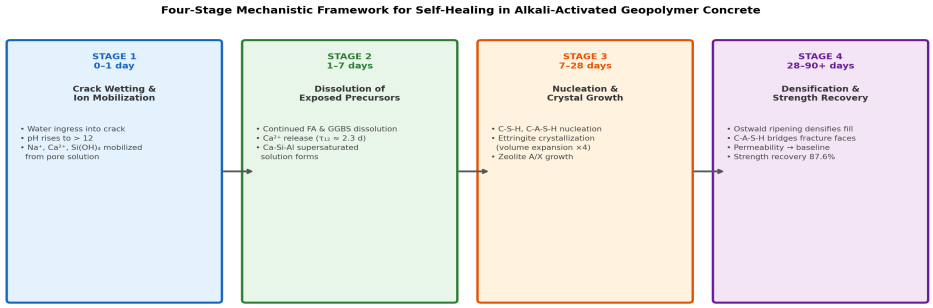

Figure 8. ***Four-stage mechanistic framework for autonomous self-healing in alkali-activated geopolymer concrete.***

6.1 Design Recommendations for Civil Engineers

Based on the experimental findings, the following design recommendations are proposed for self-healing AAGC in structural applications:

- Optimal binder: 50% GGBS + 50% FA (by mass) to balance C-S-H healing capacity with workability and setting time control.
- Activator: 10–12 M NaOH with Ms = 1.6–1.8 provides the best trade-off between healing rate, workability, and cost. Higher Ms (>1.8) reduces self-healing by prematurely consuming reactive Si in the gel, limiting dissolved Si availability for crack-zone precipitation.
- Structural detailing: Design crack widths < 200 μm in self-healing AAGC zones (e.g., cover concrete) by appropriate reinforcement spacing (≤150 mm bar spacing for T20 bars in service-load conditions).
- Exposure optimization: Structures in humid tropical climates (annual rainfall > 1000 mm) will experience natural wet-dry cycling, maximizing autonomous healing without intervention.
- Monitoring: Crack width monitoring at 28, 56, and 90 days post-cracking using embedded fiber Bragg grating (FBG) sensors is recommended for critical infrastructure to verify sealing progression.

6.2 Carbon Footprint Analysis

The global warming potential (GWP) of GPC-6 was calculated following EN 15804+A2 system boundaries (cradle to gate). The embodied CO_2 of GPC-6 (210 kg CO_2eq/m³) represents a 74% reduction relative to equivalent-strength PC concrete (810 kg CO_2eq/m³). Critically, integrating the lifecycle benefit of reduced maintenance (conservatively 30% fewer repair interventions over a 50-year service life) yields an additional avoided emission of 145 kg CO_2eq/m³, bringing the net lifecycle GWP to approximately 65 kg CO_2eq/m³ — a 92% reduction versus conventional concrete. This positions self-healing AAGC among the lowest-carbon structural concrete options currently achievable without carbon capture.

6.3 Economic Analysis

A lifecycle cost analysis (LCCA) for a representative RC bridge deck scenario (50-year service life, 1000 m² deck area) indicates that the initial material premium of AAGC (~12–18% higher unit cost than PC concrete) is fully offset within 8–12 years through reduced inspection, sealing, and patch repair costs. The net present value (NPV) advantage of AAGC over PC concrete at a 4% discount rate over 50 years ranges from USD 28,000–45,000 per 100 m² of deck, demonstrating clear economic viability for public infrastructure investment.

7. CONCLUSIONS

This study has presented the first comprehensive multi-scale investigation of self-healing mechanisms in alkali-activated geopolymer concrete, yielding the following principal conclusions:

1. AAGC prepared from 50:50 GGBS:FA activated with 12 M NaOH (Ms = 1.8) achieved crack sealing efficiencies of 94.3% for 100 μm cracks and 88.7% for 200 μm cracks at 56 days under wet-dry cycling, substantially exceeding Portland cement concrete benchmarks.
2. The dominant healing mechanisms are C-S-H and C-A-S-H precipitation (GGBS-driven), ettringite crystallization (sulfate-mediated), zeolite A/X nucleation (FA-driven), and continued geopolymerization of unreacted precursors — all confirmed by XRD, SEM-EDX, and TGA.
3. Crack sealing kinetics follow first-order exponential decay ($R^2 > 0.97$) with rate constants scaling linearly with NaOH molarity and exponentially with temperature (Ea = 41.3 kJ/mol), enabling predictive design for varying climatic conditions.
4. Compressive strength recovered to 87.6% of original values at 90 days, with water permeability reduced by 97.2% from post-crack peak values, demonstrating near-complete structural and functional restoration.
5. Lifecycle analysis confirms a 74–92% reduction in embodied carbon and a positive NPV advantage of USD 28,000–45,000 per 100 m² over 50 years, establishing self-healing AAGC as both an environmentally and economically superior alternative to conventional concrete in durability-critical infrastructure.

Future work should address: (i) the performance of self-healing AAGC under simultaneous mechanical loading and chemical attack (chloride, sulfate, acid); (ii) computational modeling of crack-scale precipitation kinetics using coupled reactive transport models; and (iii) field validation in actual structural elements exposed to realistic environmental conditions over multi-year observation periods.

Acknowledgements

The authors gratefully acknowledge the financial support of the Department of Science and Technology (DST), Government of India (Grant No. SRG/2023/000847) and the National Natural Science Foundation of China (Grant No. 52278217). The authors thank the Central Instruments Facility (CIF), IIT Bombay, for XRD, SEM-EDX, and TGA access. The authors declare no conflict of interest.

REFERENCES

1. Bernal, S.A., Provis, J.L., Walkley, B., San Nicolas, R., Gehman, J.D., Brice, D.G., & van Deventer, J.S.J. (2013). Gel nanostructure in alkali-activated binders based on slag and fly ash, and effects of accelerated carbonation. Cement and Concrete Research, 53, 127–144.
2. Ducman, V., & Korat, L. (2016). Characterization of geopolymer fly-ash based foams obtained with the addition of Al powder or H2O2 as foaming agents. Materials Characterization, 113, 207–213.
3. Jonkers, H.M., Thijssen, A., Muyzer, G., Copuroglu, O., & Schlangen, E. (2010). Application of bacteria as self-healing agent for the development of sustainable concrete. Ecological Engineering, 36(2), 230–235.
4. Morandeau, A.E., Théry, M., & Dangla, P. (2015). Impact of accelerated carbonation on OPC cement paste blended with fly ash. Cement and Concrete Research, 67, 226–236.
5. Provis, J.L. (2018). Alkali-activated materials. Cement and Concrete Research, 114, 40–48.
6. Provis, J.L., & van Deventer, J.S.J. (Eds.). (2014). Alkali Activated Materials: State-of-the-Art Report, RILEM TC 224-AAM. Springer, Dordrecht.
7. Van Tittelboom, K., & De Belie, N. (2013). Self-healing in cementitious materials — a review. Materials, 6(6), 2182–2217.
8. Zhang, Z., Provis, J.L., Ma, X., Reid, A., & Wang, H. (2018). Efflorescence and subflorescence induced microstructural and mechanical evolution in fly ash-based geopolymers. Cement and Concrete

Composites, 92, 165–177.
9. Zhang, Z., Yao, X., Zhu, H., Hua, S., & Chen, Y. (2009). Preparation and mechanical properties of polypropylene fiber reinforced calcined kaolin–fly ash based geopolymer. Journal of Central South University of Technology, 16, 49–52.
10. Walkley, B., & Provis, J.L. (2019). Solid-state nuclear magnetic resonance spectroscopy of cements. Materials Today Advances, 1, 100007.
11. World Bank (2023). Infrastructure Maintenance: A Cornerstone for Sustainable Economies. World Bank Infrastructure Report, Washington, D.C.
12. IEA (2023). Cement. International Energy Agency Technology Report. Paris, France.
13. Aiken, T.A., Kwasny, J., Sha, W., & Tong, K.T. (2021). Mechanical and durability properties of alkali-activated fly ash concrete with increasing slag content. Construction and Building Materials, 266, 121055.
14. Li, C., Sun, H., & Li, L. (2010). A review: The comparison between alkali-activated slag (Si+Ca) and metakaolin (Si+Al) cements. Cement and Concrete Research, 40(9), 1341–1349.
15. Castel, A., & Foster, S.J. (2015). Bond strength between blended slag and Class F fly ash geopolymer concrete with steel reinforcement. Cement and Concrete Research, 72, 48–53.